Comparative Studies of Mechanical Properties and Microstructure of LPBF-Fabricated Virgin and Reused 316L Stainless Steel

Wakshum Mekonnen Tucho[1(✉)], Ole Kristian Bjørge[1], Shusil Bista[1], Mette Lokna Nedreberg[2], and Vidar F. Hansen[1]

[1] Department of Mechanical and Structural Engineering and Materials Science, University of Stavanger, 4036 Stavanger, Norway
`wakshum.m.tucho@uis.no`
[2] Kongsberg Maritime AS, 6009 Ålesund, Norway

Abstract. The investigation of the various properties of components manufactured with Additive Manufacturing (AM) - methods is important to realize the implementation of recycled metals for user-end applications. This work compared the mechanical properties of virgin and recycled (green) 316L stainless steel (SS) components fabricated with Laser metal Powder Bed Fusions (LPBF). Tensile strength, Charpy-V impact toughness, and hardness tests were performed for the analysis. The specimens manufactured from the recycled 316L SS showed differences of 3–9% in hardness, 4–7% in ultimate tensile strength (UTS), and 7–8% in yield strength (YS) 0.2% compared with the virgin specimens. The difference in impact toughness between the two sets of specimens is however significant. Variations in the measurements are explained based on the studies of microstructure and phase analysis. Defects related to powders, microcracks, and compositions/phases are accountable for the differences in mechanical properties of specimens fabricated from powders of recycled metal and commercial powders. The anisotropy exhibited in the printed parts in mechanical properties and microstructure is also reported. The present work generally demonstrates that the specimens fabricated from the powders obtained from the recycled 316L SS metal can meet the standard requirements for production options and further optimization with LPBF.

Keywords: metal recycling · tensile strength · microstructure · impact toughness · 316L SS · LPBF

1 Introduction

Recycling of metals has been recently gaining the attention of industries and academia, primarily, for its economic and environmental advantages. Making new material from used scraps is regarded as a recycled or circular economy. Besides economic benefits, reusing material reduces pollution by minimizing the dumping of metallic waste. The main research area by scholars in this regard is the maintenance of mechanical integrity with minimal waste conditions. The effects of recycled metals on the quality of powder

and the various properties of the final manufactured parts need to be well understood to implement the recyclability of reused metal with Additive Manufacturing (AM) methods. Manufacturing of recycled metals with AM is however in its infancy and needs further investigations.

The production of parts of metals with the AM promotes several advantages over conventional production approaches. AM significantly cuts the production time, energy, and material consumption compared to conventional techniques, such as casting which usually requires post-processing. Nevertheless, AM-manufactured parts are characterized by defects of different levels depending on the technique employed. AM-induced defects include porosity, surface quality, and deviations from design (e.g., geometric inaccuracies), which can be occurred due to various effects related to the respective techniques. These defects are known to weaken some of the properties of the material, such as mechanical strength and corrosion resistance, which are crucial for certain applications [1–3]. Research strategies are thus aiming at minimizing or alleviating of such defects to meet the standards set for specific applications.

Published works indicate that LPBF (commonly known as selective laser melting or SLM) process is one of the most widely used AM techniques for fabricating different metals/alloys with minimal defect levels compared to other AM techniques. Stainless Steel (SS) 316L is among the most LPBF-manufactured and studied iron-based alloys. 316L SS is an austenitic chromium-nickel stainless steel with low carbon and more molybdenum than other 316 stainless steel grades. The addition of molybdenum enhances resistance to corrosion from chloride and acids, such as sulfuric, hydrochloric, acetic, formic, and tartaric acids as well sulfates [4]. This property makes 316L SS ideal for applications in marine environments where the hazards due to chloride are immensely high. 316L SS is also used for biomedical applications [5] due to its relatively superior ductility in addition to its excellent corrosion resistance in a fluid environment.

Several studies have been published recently on the recyclability of 316L SS that reported various aspects of the material. The focus of most of these papers was primarily on the effects of recycled powder properties on the manufactured parts. The physical properties of powders, including morphology, size distribution, packing density, flowability, and chemical composition are known to influence critically the microstructure and mechanical properties of the printed parts [2, 6–9, 11, 12]. For optimal powder melting and homogeneous deposition of powder layers, high packing density, and high flowability are desirable for, the LPBF process [12]. The deterioration issues related to the quality of recycled powders have been studied in detail in previous reports [12–15]. The assessment of the quality of the powder is important since the defective powder plays an immense role in the formation of pores and other defects in the final fabricated parts. Porosity is one of the most frequently observed defects in PBF methods [6, 7]. Numerous factors that are responsible for the formation of pores in LPBF have been reviewed by Malekipour and El-Mounayri [2]. These include laser specification (laser power, scan speed, and spot size); laser mode; scan strategy; balling; powder size; powder morphology; drying treatment; layer thickness; melt pool size and morphology; poor wetting; powder packing density (powder apparent density); overlapping ratio; entrapped gas; layer orientation; densification; and gas flow condition. High sphericity of powder particles is a requirement to ensure a low level of porosity as it allows for better flowability

and less surface contamination. Details are available in [2] and in the references cited thereof.

As briefly shown above, most of the reports in the literature on AM-recycled 316L SS and other alloys have been focussing on the changes of various properties of as-received powders after one or several recycling in the build chamber. In this study however, the powder studied was manufactured from scraps of recycled material. Hereafter, we refer the components based on the scraps of used 316L SS as 'green'. The reusing of green materials is very beneficial since it reduces the usage of natural resource in addition to lower waste and less emission. According to the American Iron and Steel Institute [16], one ton of recycled steel saves about 2,500 lb of iron ore, 1,400 lb of coal, and 120 lb of limestone. Considering this, the current work attempts to insight into the benefits of combining additive manufacturing with the recycling of materials. For the investigations, the scraps of used 316L SS were first made into powders and then printed using the LPBF method. The analysis involves characterization of powders, microstructure, and mechanical properties of the printed components. The LPBF-fabricated parts from the powders obtained from the green are compared with that of commercial (virgin) powders of 316L SS in terms of tensile strength, hardness, and impact toughness measurements. In addition to the variations in composition, defects such as porosity and microcracks are analysed qualitatively and quantitatively for justifications.

2 Materials and Experimental Methods

2.1 Powder

Stainless steel 316L is a highly corrosion-resistant with a minimal contamination uptake when it is in contact with other elements. Because of this, 316L SS is a sustainable alloy for recyclability, and it is thus regarded as a "green" material. The "green" powder was produced by RINA Consulting CSM (Italy) using Vacuum Induction Gas Atomizing (VIGA) system, whereas f3nice (Milan, Italia) has initiated the conversion of greens of metals into atomized powders to produce parts with the LPBF system.

The powder considered 'green' in this work is a mixture of 90% powder fabricated from reused material and 10% of commercial material. Hereafter we refer as 'green powder' to distinguish it from the commonly used term 'recycled powder' adopted in the literature. The term 'virgin' will be used to refer to the powders and components manufactured from commercial 316L SS. The typical scraps of green material of 316L SS are shown in Fig. 1. The nominal chemical composition of the pre-alloyed 316L SS is shown in Table 1. Before feeding into the VIGA system for powder production, the green materials were thoroughly cleaned to remove contaminants. For comparison, the chemical composition of both virgin and green powders was measured using Inductively Coupled Plasma (ICP) method.

2.2 Materials

The 316L SS specimens of both virgin and green were fabricated by AIDRO (Milano, Italy) using a single laser LPBF (EOS M290) machine. The printing parameters were

Fig. 1. Scraps of green 316L stainless steel.

Table 1. Composition of 316L SS powder based on ASTM F138–19 standard.

Elements	Virgin		Green	
	min	max	min	max
Cr	17	19	17	19
Ni	13	15	13	15
Mo	2.25	3	2	3
Mn	–	2	–	2
P		0.01	–	0.025
S	–	0.01		0.01
Cu	–	0.5	–	0.5
Co	–	0.1		–
Si	–	0.75	–	1
N	–	0.1	–	–
C	–	0.03		0.03
Fe	Bal		Bal	

so adjusted to a volumetric energy density of 58 J/mm^3 following the recommendation of the machine manufacturer. The laser scan rotation between each layer (40 µm) was about 50º during printing. The number and dimensions of specimens fabricated were in accordance with the DNVGL-ST-B203 standard and a 3D model shown in Fig. 2(a). The

virgin and the green powders were deposited under similar printing conditions, including process parameters. The specimens for the tensile test were labelled based on the building orientation as shown in Fig. 2(a, b). These are XX (x-direction), YY (y-direction) and ZZ (z-direction) (labelled A, B, C, D and E). The latter specimens (ZZ) were also labelled with subscripts T (top) and B (bottom) to indicate relative positions in the building direction. An example is AT and AB for the specimen labelled 'A'. The length and diameter of these cylindrical specimens are 100 and 12 mm, respectively. For comparative analysis, the tensile measurement was performed on both top and bottom parts of the virgin material. Only the bottom (subscripted as B) sections of the Z-specimens were tested for the green.

For hardness, microstructure and porosity analysis, a cube (labelled as CB20) of (20 × 20 × 20) mm^3 (Fig. 2c) was printed one each, for both virgin and green. Specimens for impact notch toughness tests were printed following the standard dimensions of (55 × 10 × 10) mm^3 adapted from ISO 148-1:2016. Three specimens (e.g., XX1, XX2 & XX3 for x) for the three orientations (X, Y and Z), i.e., nine specimens in total for each of the virgin and the green were printed for measurements of impact toughness tests.
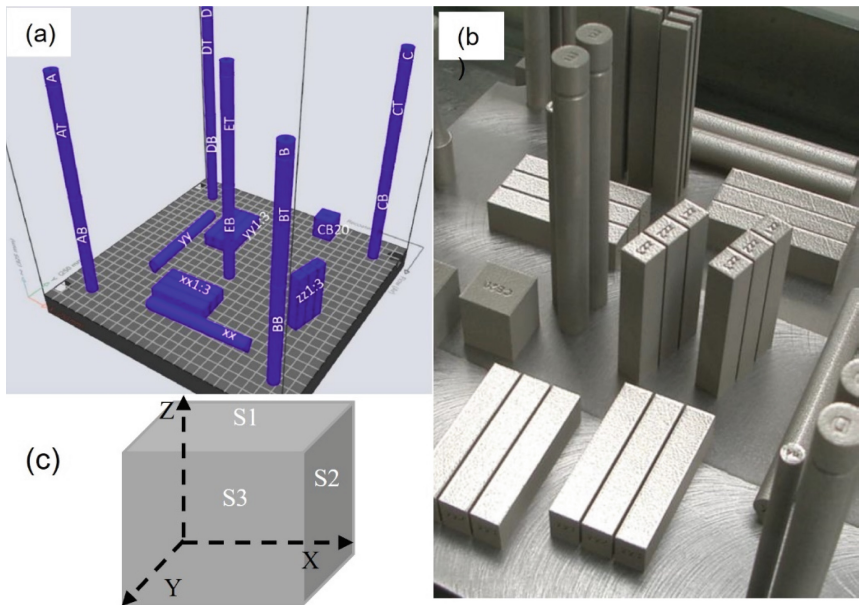

Fig. 2. Components printed using both virgin and green powders (a) orientation and relative positions of the specimens on the building platform, (b) fabricated specimen, and (c) a cube (CB20) used for hardness and microstructure analysis.

2.3 Tensile, Impact and Hardness Testing

For the tensile tests, specimens were prepared following ASTM E8 standard using Computer Numerical Control (CNC) machine (Mazak Smart 430A). A schematic and the

samples machined based on the dimensions provided are shown in Fig. 3. Tensile test was performed using an Instron 5985 universal tensile testing machine (Norwood, US) which has a maximum loading capacity of 250 kN at a strain rate of $0.00007\ s^{-1}$.

The Charpy impact toughness testing was performed using a Charpy V-notch test system (Zwick/Roell). at room temperature following ISO 148-1:2016 standard. For the impact tests, the notches for the x- and y- oriented specimens were formed parallel to the build direction, whereas the notches of the z-built specimens were normal to the building direction (BD) following DNVGL-ST-B203 specification. CNC machine was used for grounding the notches (the specimens are listed in Table 2, column 3).

Table 2. List of tensile and impact specimens relative to the building directions

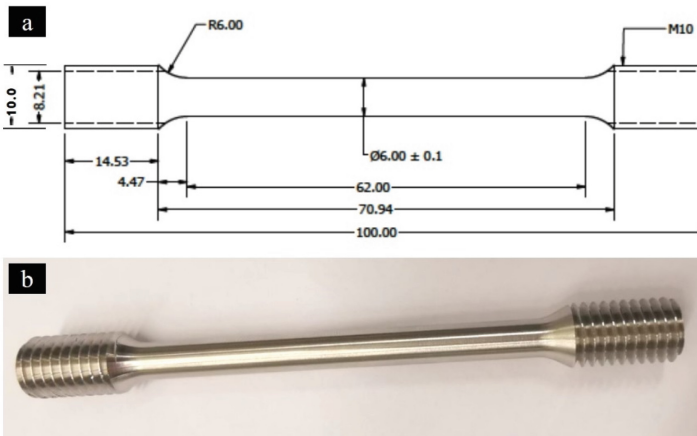| Orientation	Tensile	Impact
X	XX	XX1
		XX2
		XX3
Y	YY	YY1
		YY2
		YY3
Z	A, B	ZZ1
	C, D	ZZ2
	E	ZZ3

Fig. 3. Tensile specimen (a) dimensions and (b) typical specimen after machining.

Hardness tests were performed using a Vickers NOVA 330 (Struers, Denmark) testing machine under 10 kg HV force for a dwell time of 10 s. Surfaces of the specimens were

finely polished according to the requirements for Vickers hardness testing. The hardness measurements were done on three orthogonally oriented surfaces shown in Fig. 2(c). The interval between adjacent indentations was 1 mm. The closest indentation to the edge was about 3 mm. The average hardness was calculated from at least 10 measurements for each of the specimens tested.

2.4   Characterization of Microstructure

The microstructure of the samples sectioned from the printed specimens was analysed with light optical microscopy (LOM, Olympus GX53, Germany). In addition, the microstructure, composition, and fracture surfaces of the specimens were analyzed with Scanning Electron Microscopy (SEM), Gemini SUPRA 35VP (Carl Zeiss, Jena, Germany) equipped with EDAX Energy Dispersive X-ray Spectroscopy (EDS). Sample preparation for microstructure analysis consisted of mechanical grinding, fine polishing, and ultra-fine polishing with OP-S colloidal silica. For observation with LOM, the samples were electro-etched with Struers Lectropol-5 (Struers, Ballerup, Denmark) at 15 V for 15–20 s in a 10% aqueous oxalic acid solution. Phases and lattice defects were further investigated with Transmission Electron Microscopy (TEM), JEOL-2100 (LaB6 filament) (JEOL, Akishima, Tokyo, Japan), operating at 200 kV. For TEM analysis, thin foils were prepared, first by thinning down mechanically to a thickness of about 100 μm, and then 3-mm disks were punched from the thin foils. These disks were then electropolished using a dual jet polishing system Struers TENUPOL-5 (Struers, Ballerup, Denmark) operated at 15 V and −30 °C in an electrolyte solution of 95% methanol and 5% perchloric acid.

3   Results and Discussions

3.1   Powder

The composition of the powders was analysed based on ASTM E1019-18 standard using ICP chemical analysis method by AIDRO (Milano, Italy). The numerical values are tabulated in Table 3. The result shows slight differences in composition between the two types of powders for most of the elements, but both are within the limit set by the standard (Table 1). Co is not detected in the green powder, but additional elements (V and Ti) were seen at very low concentrations. These elements are not in the list of the standard composition of 316L SS shown in Table 1. Their impacts are however considered negligible since they are very low in concentration.

SEM images of both virgin and green powder particles and Powder Size Distribution (PSD) are shown in Fig. 4. A closer examination of the images in Fig. 4(a) and (b) reveals that the particles of both powders exhibit similar morphology. Both virgin and green powders contain combination of spherical and deformed particles of various sizes. Particles with satellites are also available in both powders (Fig. 4a & b). Quantitative analysis, such as sphericity measurement is however required to determine the differences. Based on their studies of LPBF SS 15-5 PH recycled powder, Zhang et al. [17] proposed the repeated heating/cooling cycles during processing and increased interparticle friction during powder bed recoating for the causes of the rougher texture. The

Table 3. Chemical composition of a virgin (v) and green (g) powders in wt.%.

Element	virgin	green
C	0.021	0.013
O	0.047	0.066
Al	0.01	0.01
Si	0.37	0.4
P	0.014	0.016
Mo	2.85	2.84
S	0.007	0.008
Cr	17.49	18.02
Mn	1.54	1.52
Ni	13.86	13.99
Cu	0.05	0.03
N	0.07	0.09
Co	0.03	–
Ti	0.01	0.01
V	0.03	0.03

underlining phenomenon for the occurrence of roughness related to a very fast heating/cooling process is assumed to be the resulting stresses due to expansion-contraction effects.

Besides composition analysis, particle size distribution and morphology may have important effects on the microstructure of the fabricated parts. Figure 4(c) shows the PSD curve of virgin and green powders. The average particle sizes (D50) of the virgin and green powders are quantified based on the cumulative volume distribution fraction shown in Fig. 4(c). The measurement shows that the values of D50 for virgin (37.4 µm) are slightly larger than that of the green (34.7 µm) powders. The higher D50 values for the virgin powders in this study is contradicting those obtained for various recycled AM metal powders observed in other studies [10, 18]. The virgin powder also exhibits a wider range of PSD than the green powder. Nevertheless, the difference in particle size and shape between the green and virgin powders is not so significant. The green powders have thus shown similar morphology and dimensions as that of the virgin powders. It is because the green powders in this study are different from the recycled powders in the literature that experienced a few or several cycles of recycling before being printed.

3.2 Composition of Fabricated Specimens

The elemental composition of both virgin and green specimens was analysed using SEM/EDS system, and the results are presented in Table 4. A substantially large area (about 3.5 mm × 2.5 mm) was scanned for the EDS analysis in each specimen. Significant
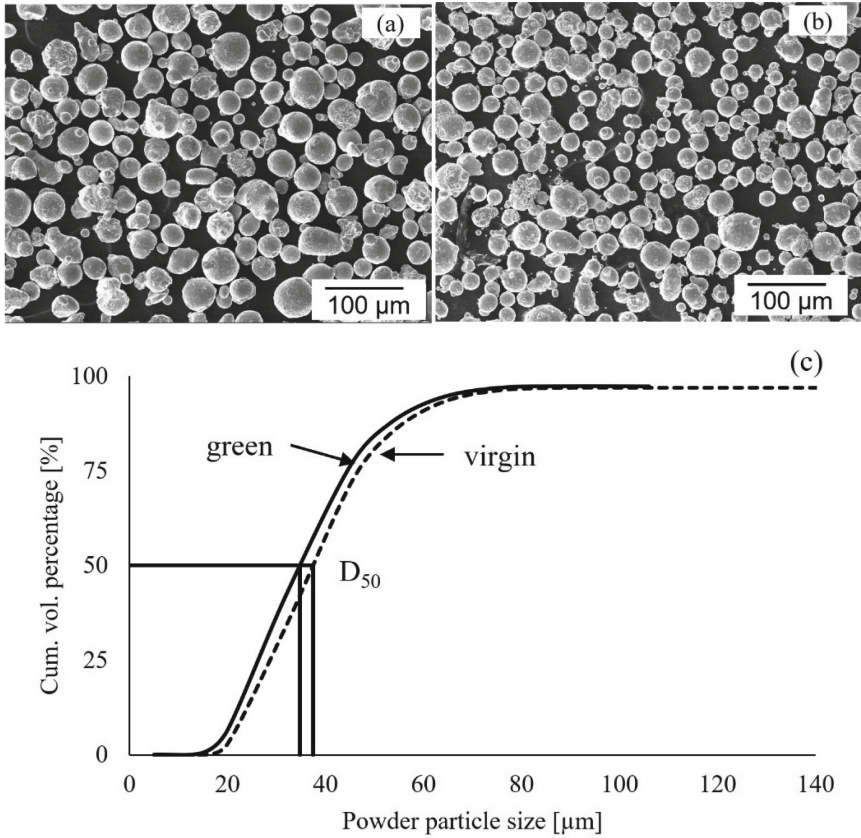
Fig. 4. SEM images of (a) virgin powder, (b) green powder, and (c) cumulative volume fraction that show particle size distribution.

differences in composition were observed for certain elements as shown in Table 4. The fourth column in the table shows the difference in wt.% (g-v). The green specimen contains a slightly larger quantity of the alloying elements, including Fe, Cr, Cu and Ni than the virgin specimens. In contrast, the virgin contains slightly larger quantities of Mn, Mo, C and O. As we shall see in sub-Sect. 3.4, considerable quantities of nanoparticles rich in Si and O are observed in the matrix. The impacts of the main elements on the various properties of the material are based on the concentration limits set by the standard. The difference in Si concentration is significant (ca. 1.4 wt.%), i.e., 2.0 and 0.59 wt.% for virgin and green specimens, respectively. Ca is undesirable element, but its concentration is very low in both specimens.

3.3 Microstructure

To illustrate the scan strategy and the profile of the melt pools, typical images of OM are presented in Fig. 5. The images were recorded from surfaces normal and parallel

Table 4. Elemental composition (wt.%) of virgin and green specimens.

Element	v	g	g - v
C	8.92	7.75	−1.17
O	6.42	5.75	−0.67
Al	0.48	0.55	0.07
Si	1.99	0.59	−1.4
P	0	0.03	0.03
Mo	1.66	1.62	−0.04
S	0.07	0.08	0.01
Ca	0.04	0.01	−0.03
Cr	15.31	15.76	0.45
Mn	1.22	1.06	−0.16
Fe	52.56	54.83	2.27
Ni	11.27	11.59	0.32
Cu	0.05	0.39	0.34

to the BD. As shown in Fig. 5(a), the laser tracks appear closely packed in different orientations. The average width of the track is about 95 µm, which is approximately equal to the melt pool size (~100 µm). After completion of each layer, the scanning direction changes by 50° to make the three orientations seen in the image by black arrows. The white arrow indicates the orientation of the fourth layer which is not visible in the image. The image in Fig. 5(b) illustrates the profile of melt pools and the growth direction (white arrow) of grains relative to the BD. The melt pools have different shapes depending on the orientation of the scan tracks shown in Fig. 5(a). As a result of this and overlapping nature, only a few of the melt pools appear with full semi-circular shapes. Most of the grains grow epitaxially in the BD and are normal to the fusion lines. The white arrow in Fig. 5(b) is pointing along some of the elongated grains that cross several melt pools. Such growth behaviour of the grains normally results in texturing. The high energy melting results in a large and deep melt pool that consists of columnar grains. As more layers are involved during remelting at ultra-high heating/cooling rate conditions, it promotes epitaxial grain growth and a sharp texture with oriented grain.

The fabrication process of additive manufacturing generally involves a very fast heating and cooling rates as compared to the conventional techniques. This results in the microstructure of LPBF-fabricated 316L SS being different from that of the as-cast and the wrought ones. The grain morphology of the LPBF fabricated-316L SS can be columnar, equiaxed, or irregular as reported previously [3] and shown in Fig. 6. The EBSD coloured grain maps of the surfaces normal to the BD (Fig. 6 a & b) reveals equiaxed and irregularly shaped grains for both virgin and green specimens. On the other hand, the images of the surfaces parallel to the BD exhibit elongated and coarser columnar grains compared to the grains of the surfaces normal to BD (Fig. 6c & d).
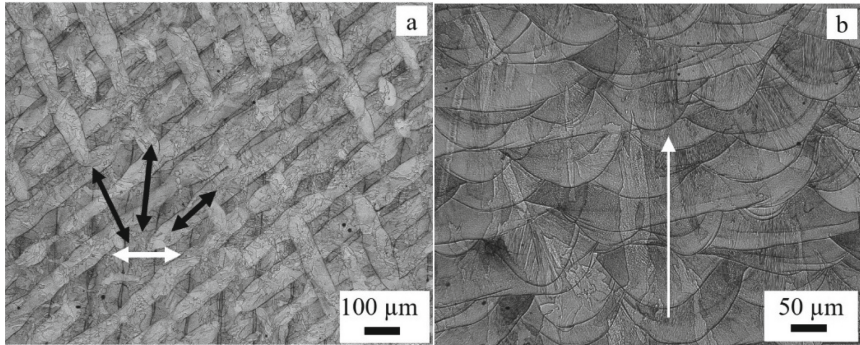
Fig. 5. Optical microscopy images of the green specimen (a) normal (S1-parallel to the scan plane) (b) parallel (S3 – normal to the scan plane) to the BD (see Fig. 2c). The arrow in (b) indicates the growth direction following the grains that cross several fusion lines in the BD. The double arrows in (a) show the orientation of the layers.

The shapes of the grains are described relative to the viewing directions. There are also many fine grains around the coarser ones. The EBSD images exhibit that grain morphology shown in Fig. 6(a) and (b) can be mainly the cross-sectional view of the grains shown on the surfaces parallel to the BD. It means that most of the grains are columnar and appear larger in number than the equiaxed grains. Furthermore, as shown in Fig. 5(b), the columnar grains appear perpendicular to the center of the melt pool which experiences a large temperature gradient. This is in line with the formation mechanism of grain morphology which is often described by the ratio of temperature gradient (G) to solidification rate (R). The supercooling theory [19, 20] shows that an increase in G and a decrease in R favours the growth of equiaxed grains. Likewise, an increasing R and a decreasing G case can lead to the growth of columnar grains.

Figure 7(a) and (b) depict a high degree of crystallographic features where the grains of both virgin and green specimens are preferentially oriented in 101 directions for the surface normal to the BD. However, the green grains mapped parallel to the BD show a tendency of texturing in the 001 direction. Whereas the grain of the virgin specimen has shown a random orientation related to the BD. Literature [21] indicates that the 001 direction has the lowest Young's modulus in fcc systems for austenitic steels. Thus, the preferred orientation of the grains in the 001 direction is accompanied by a reduced Young's modulus.

Detailed examination of the as-printed LPBF-fabricated parts with TEM reveals that grains generally contain columnar and cellular subgrains. Typical TEM images of cellular subgrains are shown in Fig. 8(a) virgin and (b) green. The subgrain boundaries are known to impede the sliding of dislocations and form a high density of dislocations pileups. As shown in the images, the grain boundaries are enriched in a higher density of dislocations compared to the interior of the subgrains for both virgin (a) and green (b) specimens. It is the sub-grain structures and its content that make the AM-manufactured materials different from the conventional materials. The strength of the as printed parts at the optimum processing condition is usually higher than the conventional material because of the high stresses in the sub-grain structures. Subgrain boundaries of some
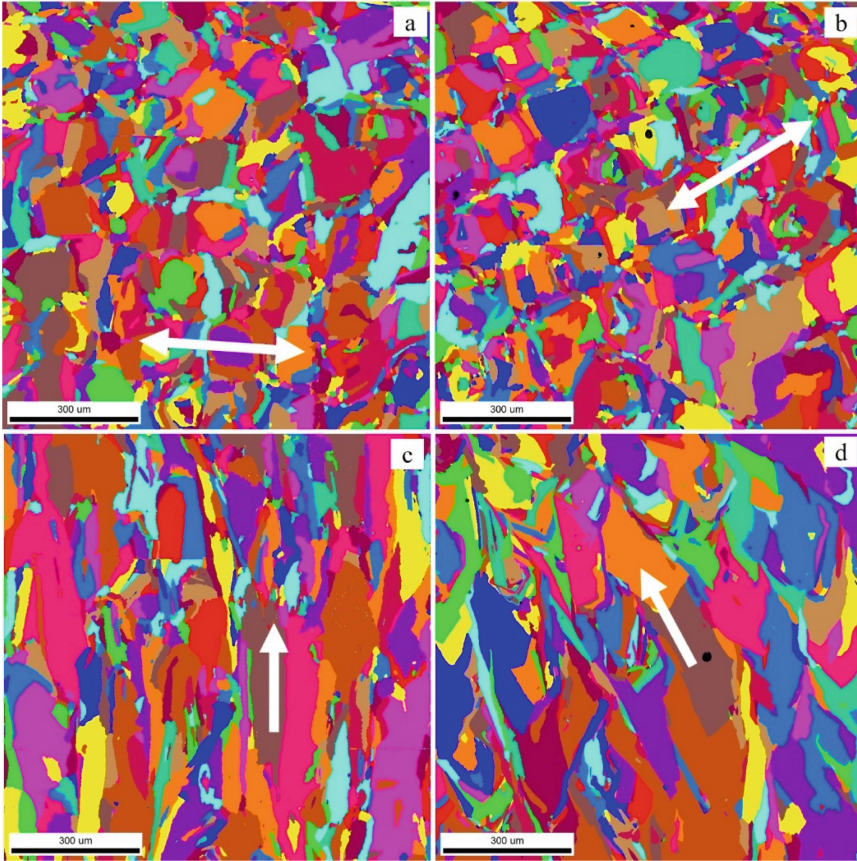
Fig. 6. EBSD grain maps of (a) v-normal, (b) g-normal, (c) v-parallel and (d) g-parallel surface with respect to BD. The arrows in (a) and (b) indicate the scan track orientations, whereas those in (c) and (d) show building directions. The scale bars in all images are the same and 300 μm long, each.

alloys, such as Inconel 718 consist not only of dislocations, but they are also decorated with a high density of segregated nano-particles that further strengthen the material [22, 23]. Segregated elements in the subgrain boundaries of the LPBF-316L SS is however very low.
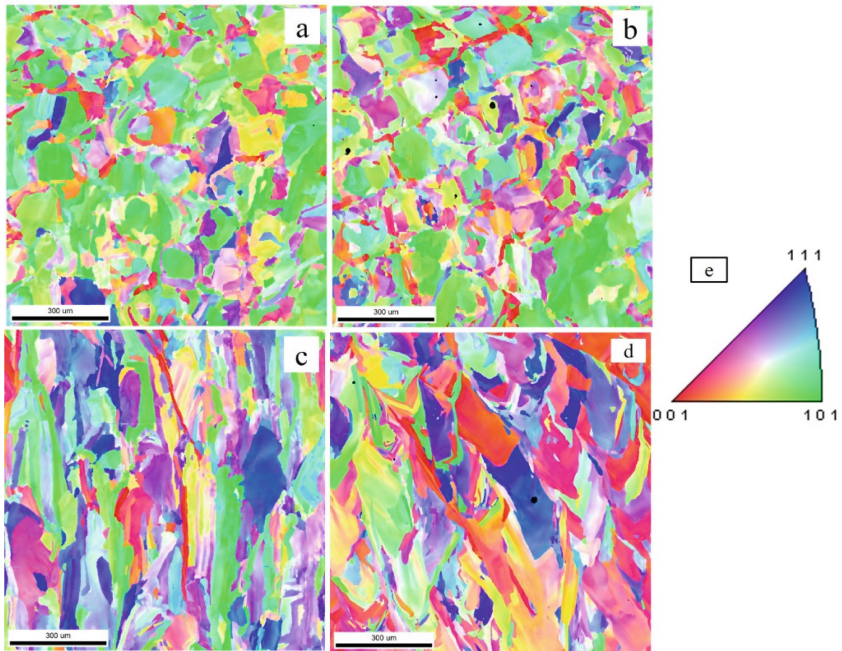
Fig. 7. IPF (a) v-normal, (b) g-normal, (c) v-parallel and (d) g-parallel surface with respect to BD and (e) IPF colour key.
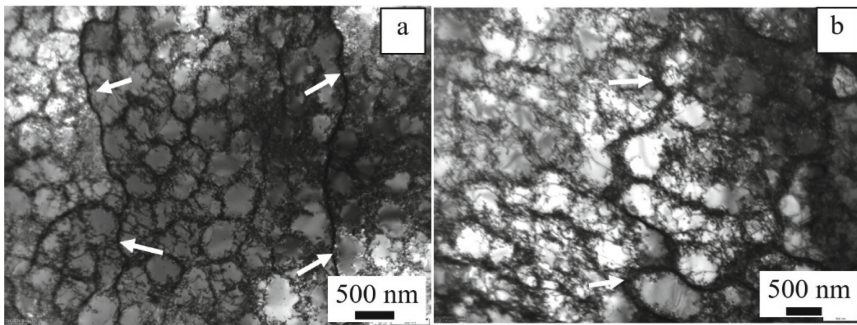

Fig. 8. TEM images of the as printed (a) virgin and (b) green samples. Both images show sub-grain structures. The subgrain boundaries are characterized by a high density of dislocations and segregated particles (rarely). The arrows in the images are pointing to grain boundaries.

3.4 Defects

Porosity, lack of fusion (LOF), and cracks are the main defects identified in the parts fabricated by the LPBF process [24] that can substantially affect the mechanical properties of metals. The cuboid parts were analyzed qualitatively/quantitatively using SEM images to characterize the defects.

Microcracks

Microcracks and a lack of fusion-type defects were observed in both virgin and green specimens. However higher density of microcracks is seen in the green specimens than in the virgin specimens. The concentration of microcracks observed are higher around the edges than in the interior regions of the specimens. Typical SEM images acquired from
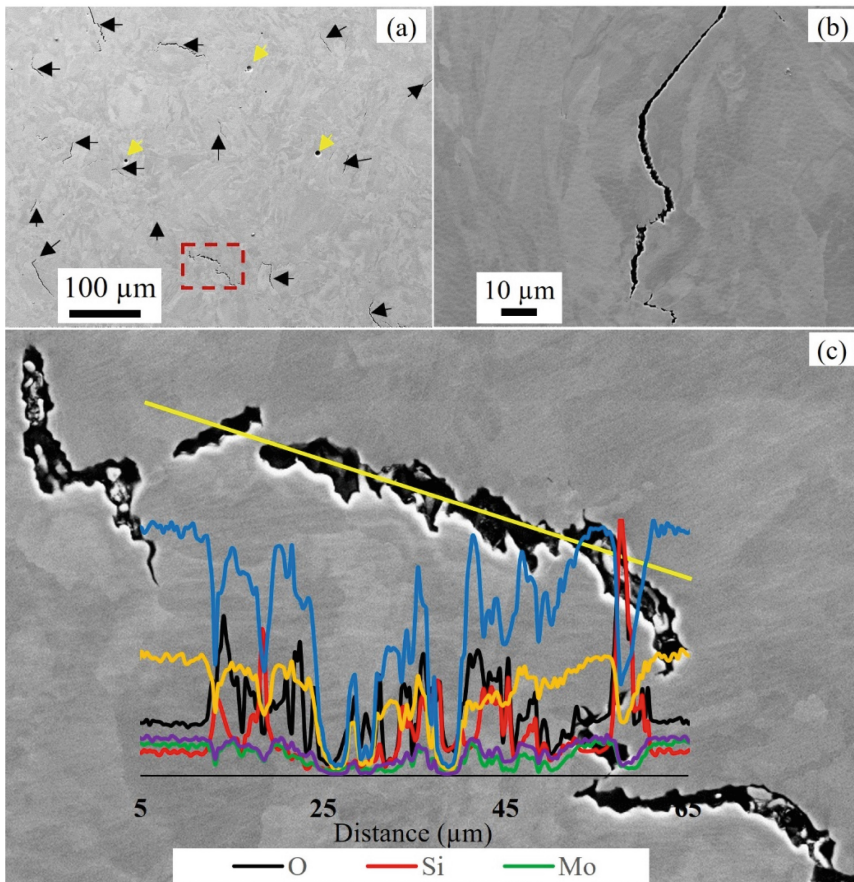

Fig. 9. Microcrack/LOF defects in the green specimen (a) in transverse view at low magnification, (b) parallel view with respect to BD, and (c) magnified image of a region marked with a rectangle in (a). The black arrows in (a) are pointing to some of the microcracks, whereas the yellow arrows are pointing to spherical pores. The inset in (c) is an SEM/EDS line scan along LOF and the composition spectrum of O (black), Si (red), Mo (green), Cr (yellow), Fe (blue), and Ni (purple).

the green specimen are shown in Fig. 9(a). The microcracks are mainly transgranular that do not run along any of the interfaces (Fig. 9b). Only a few of them were found intergranular-type cracks that run along the grain boundaries. Lack of fusion defects is often seen with unmelted powders or particles (Fig. 9c). Most of these defects are rich in Si and O compared to the concentration levels in the matrix. EDS line scan that illustrates the composition profile of such defects is shown in the inset of Fig. 10(c). The concentration of Si and O observed in the cracked region is higher than that of the matrix. The concentrations of Fe, Ni, Cr, and Mo are however depleted in the crack regions.

The microcracks depicted in Fig. 10 lie at or/and close to the unmelted powders. They seem to originate from the unmelted powders and run further into the matrix. It is unknown if such cracks are inherent in the powders or introduced during the printing process. The initiation and propagation of microcracks in LPBF fabricated parts are however due to the combined effects of a very high-temperature gradient and great residual stresses [25, 26]. LPBF-fabricated stainless steels and Ni-based superalloys are highly susceptible to crack formation due to their low thermal conductivity and high thermal expansion coefficient [24]. The causes for such defects are lack of fusion due to low energy input locally during printing that results in insufficient melting of the powders. The review paper by Zhang et al. [24] summarizes two types of lack-of-fusion defects. These are defects with unmelted metal powders (Fig. 9c) and poor bonding due to insufficient molten metal. The latter occurs due to insufficient penetration depth as a result of incompelete melting of powders that leads to poor interlayer bonding. Powders remain unmelted when the laser energy input is not high enough, such that the width of the molten pool becomes small and leads to insufficient overlap between scan tracks. It is thus very difficult to remelt these powders in the printing of a new a layer to form an incomplete fusion hole that becomes inherent in the fabricated parts. Additionally, the causes/intensification of the microcracks can be related to the oxide layers that are identified with EDS as shown in Fig. 9(c). The presence of thick oxide layers can prevent the occurance of compelte bonding of layers [27]. Such region with weak bond can then leads to microcrack. Careful tuning of the LPBF printing parameters, including laser power, scan speed, hatch spacing, thickness layer, chamber environment, and powder material can effectively minimize occurrences of the defects. Details can be referred in the review article by Zhang and co-workers [24]. Propagation of the microcracks can also be enhanced by chemical segregation.
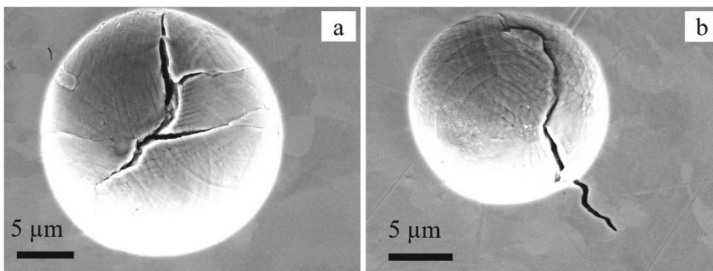

Fig. 10. Microcracks associated with unmelted powders in the green specimen.

Porosity

Porosity is one of the most observed defects in the AM-fabricated components that leads to poor material density. Although the LPBF fabricated components are seen as the highest material density compared to other AM methods, they often consist considerable amount of porosity. In the current study, we have analyzed porosity using several SEM images from both specimens (virgin and green) as shown in Fig. 11. The maximum size of these pores is 1.2% per sample/image for virgin and 0.42 for green specimens. Likewise, the average porosity of virgin and green specimens is 0.47 and 0.16, respectively.

Most of the pores observed in the virgin material are spherical in shape which is intermittently observed in the specimens studied (Fig. 9(a)). As shown in previous studies, for example [28], spherical pores are likely to be created due to the trapped gas inside precursor powder. The review article by Zhang et al. [24] gives an overview of powder-related porosity. The packing density of the metal powder is normally low (about 50%) due to low sphericity of the powder particles. As a result, large volumes of void spaces are retained in powder-hold gases. These gases were dissolved into the molten pool during printing. Due to the high cooling rate during solidification, the gases couldn't escape from the molten pool, and they are transferred to the fabricated part to form pores eventually. The formation of irregular pores, is often associated to the unmelted powder or non-fussed particles that occurred due to insufficient or excessive powers as pointed out by Sames et al. [29].

The pores observed in both materials are relatively low. However, the virgin material consists relatively a higher percentage of porosity than the green material. As indicated above, the gases can be picked up during the powder atomization and/or manufacturing process. It is believed that most of the unmelted powder particles might be exposed to the gases multiple times before being melted and integrated into the part being built during the recycling in the building chamber. The pores can also be formed by the reactions between O and C which are present in small amounts during printing processing, causing CO or CO_2 gas entrapment in the LPBF-built parts [28, 30]. The oxide thus acts as a nucleation site for pore formation, stabilization, and growth [31].
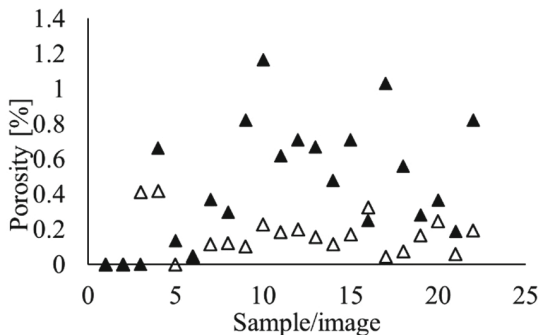

Fig. 11. Average percentage porosity per surface/image - solid triangles represent virgin, whereas the open triangles refer to the porosity in the green specimens.

Nanoparticles

The nanoparticles observed in both virgin and green specimens are rich in Si and O relative to the composition of the matrix. These nanoparticles are seen as circular that can be spheres or disks. An example of an SEM image of the precipitates formed in the virgin specimen is shown in Fig. 12(a). Most of them are smaller than 100 nm, but a few of them measure as large as 0.5 µm in diameter. They are randomly spread throughout the entire volume of the specimens. Qualitative observation indicates that the density of precipitates is higher in the virgin material than in the green material. This is consistent with the chemical composition of the specimens presented in Sect. 3.2. As shown in Table 4, the concentration of O and Si is significantly high in the virgin specimens compared to that of the green specimens.

The EDS/SEM point analysis on one of the nanoprecipitates labelled as '1' and the matrix labelled as '2' are shown in Fig. 12(b). The precipitate (1) contains a higher concentration of O and Si than in the matrix (2). The wt.% of Si and O from point (1) are about 1.07 and 3.89, respectively. Oxygen is not detected at location 2 (matrix) but a lower concentration of Si (0.36 wt.%) was measured. The concentration of Si and O however depends on the size of the precipitates. The larger precipitates contain as high as 15 wt.% O and 10 wt.% of Si. Since Si shows a higher chemical affinity for oxygen than the rest of the elements in the 316L SS, it reacts easily with the residual oxygen in the building chamber to form oxide particles. The mechanism related to the formation of oxide particles is well discussed in [3]. The spherical nanoparticles are believed to be
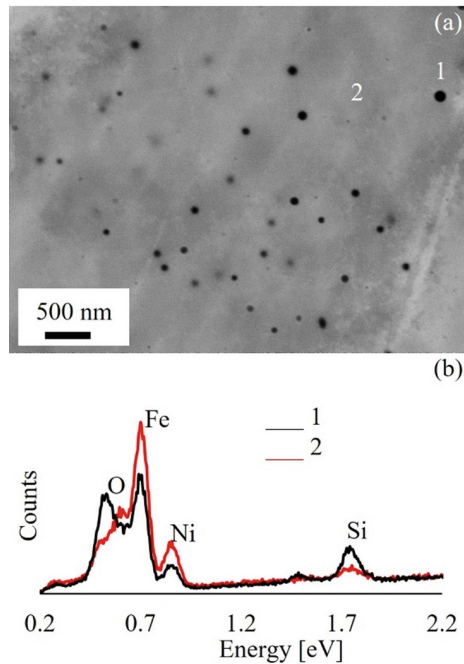

Fig. 12. (a) typical oxide of nanoprecipitates observed in virgin specimens, (b) EDS spectrum of point analysis of location 1 (precipitate) and 2 (matrix).

very effective in hindering dislocation movement. Before the test, if the specimens were heat treated at a moderate temperature as shown by Chen et al. [32], the mechanical strength of the specimen could be reduced since the precipitates are dissolved. Hence, having a reasonable volume fraction of such oxide nano-particles in the 316L SS is considered an advantage since it enhances hardness and tensile strength [33, 34].

Hardness Test

The average harnesses of both virgin and green specimens are plotted and shown in Fig. 13 to visualize the differences between the two sets of specimens. As illustrated in Fig. 1(c), S1 is a surface normal to the BD, while S2 and S3 are surfacing parallel to the BD, but with different orientations. The measurement indicates that the virgin samples are generally harder than the green samples. In particular, the hardness of S2 and S3 of the virgin material is larger than their green counterparts by 7 and 19 HV, respectively. In terms of percentage S2(v) exceeds S2(g) by 3%, while S3(v) exceeds S3(g) by 9%. The differences in hardness between the virgin and green specimens are believed to be due to differences in the defect levels presented in the previous sub-sections. A larger number of micro-cracks and microvoids were observed in the green specimens than in the virgin specimens which would be accountable for the variations in hardness measurement. The impact of the oxides wouldn't be ruled out as well. Oxides as indicated above can reinforce hardness.
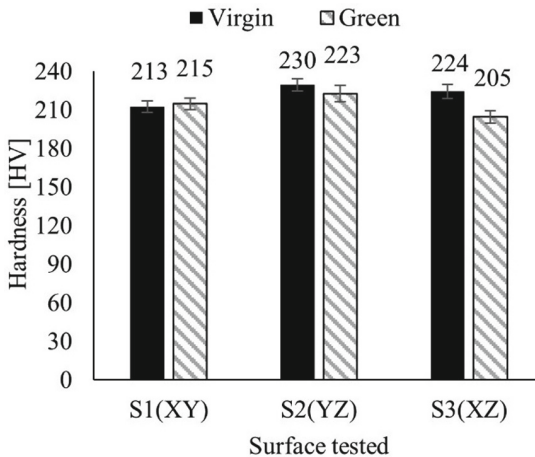

Fig. 13. Hardness measurement of virgin and green specimens. The black solid bars represent the virgin specimens, and the patterned bars are for green specimens. The labels shown above the bars are the average hardness in HV.

The difference in hardness (2 HV) measured on the surfaces normal to the BD (S1) between the virgin and the green specimens is insignificant. However, the hardness is anisotropic as they exhibit variations on different surfaces for both specimens. S2 (YZ) faces appearing harder than the other two faces (S1 and S3) for green and virgin specimens. This is due to the inhomogeneity in the microstructure that leads to the

anisotropic nature of hardness on different surfaces with the same specimen. Overall, the hardness values of the recycled and virgin specimens are comparable with reports in the literature, for example [3].

3.5 Charpy V-Notch Impact Test

To assess the ability of absorbing sudden and concentrated energy before fracture, the specimens were subjected to a Charpy impact toughness test. The virgin specimens have absorbed larger energy than the green specimens as shown in Fig. 14. Among the largest differences between the virgin and green specimens in impact toughness observed is between the specimens built in the vertical orientation. The largest and the smallest average energy absorbed by the virgin and green specimens before fracture is 139 J and 71 J, respectively. The difference between the two sets of specimens (VZ & RZ) is about 68 J (96%). The least energy differences observed are between the X-oriented specimens, which is 28 J (28%). In general, the observed differences between the two sets of specimens are significant. For the virgin material, the vertically built (Z) specimens have larger impact toughness than the horizontally built specimens (X- and Y-). Contrary to the virgin specimens, the largest impact toughness attained by the green material is the horizontally built (X) specimens.
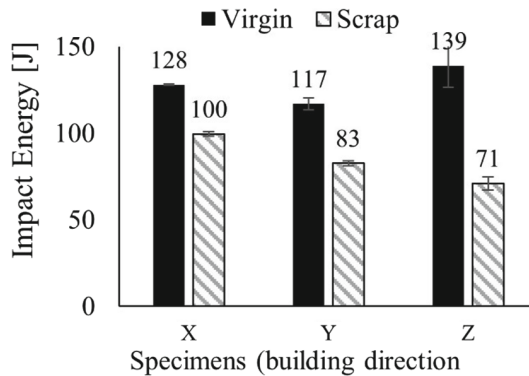

Fig. 14. Average impact toughness of virgin and green specimens built in different orientations.

It is desirable to have a material with high impact toughness with a good combination of strength and ductility. Hardness is positively correlated with strength [35], but roughly speaking, hardness/strength is negatively related to ductility. However, there is a trend for ductility to be related positively with impact toughness. A material with the longest elongation can generally attain the largest impact toughness. Impact toughness is thus more dependent on ductility variation than on hardness/strength as shown by Neikter et. al. [36] in a similar approach. The trend of the impact toughness of the virgin specimen is consistent with the reports in the literature. The specimens with the longest elongation (Z-built) as shown in Fig. 17, have absorbed the highest impact toughness (Fig. 14). The green specimens however behave the opposite. The specimen with the shortest elongation (X-) has shown the highest impact toughness. For the green specimens, the

one with the highest ductility is the vertically built specimens (Z), but they are the ones with the least impact toughness. Compare with the results of Fig. 14 and Table 5.

The typical impact fracture surfaces of the virgin and green specimens are shown in Fig. 15. All the surfaces analyzed are characterized by microcracks that are nearly running perpendicular to the applied stress. The cracks seen in the low magnification images of Fig. 15(a) virgin-Z and (b) green-X are perpendicular to the applied stress. Following the illustration by Fu and Zhang [37], these cracks are assumed to be running along the grain boundaries. When the grain boundary is perpendicular to the applied stress, the resulting initiated cracks tend to propagate along the grain boundary with increasing external stress. The crack propagation naturally follows the direction of the grain boundary since its movement is hindered by grains. Furthermore, under external stress, the triple junctions become easy sites for the stress concentration that leads to crack initiation and propagation along the grain boundaries. After a lengthy propagation time along the grain boundaries, the crack penetrates the interface between brittle inclusions and grain boundaries until the fracture occurs as shown by Fu and Zhang [37].

Figure 15(c) virgin and (d) green show regions with dimples and coalesced areas. Generally, the fracture morphology and the cracking behaviour of the specimen suggest a transformation of ductility to the brittleness nature of fractures. The cracks are transgranular type, due to the high impact force. The crack initiation zone consists of both ductile dimples and cleavage facets that indicate a mixed fracture behaviour. The fact that the green specimen demonstrates lower impact toughness is believed to be due to the pre-existing microcracks that became the initiation sites and propagation for the
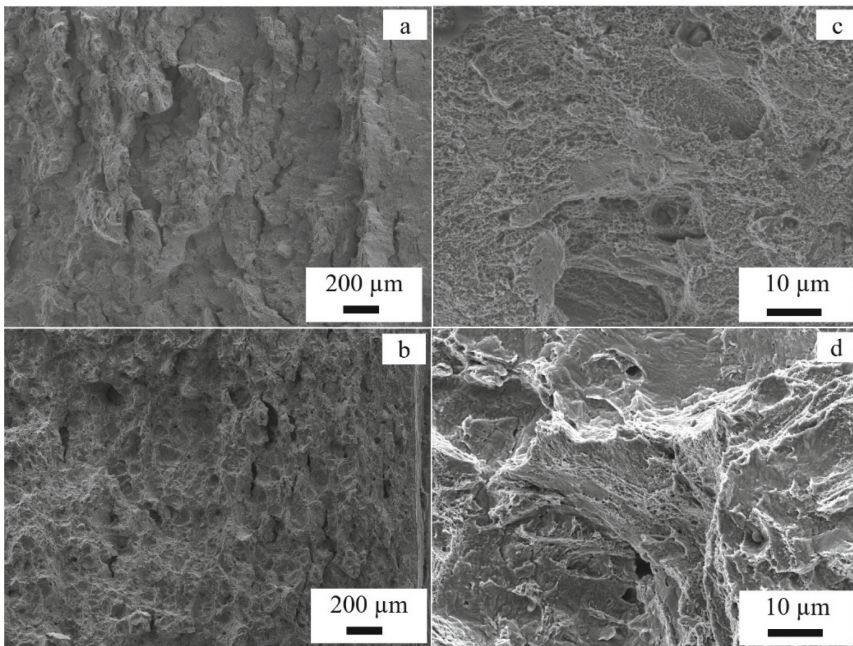

Fig. 15. Examples of impact fractures: (a) virgin-z, (b) green-X, (c) virgin-Z and (d) green-X.

lower plasticity nature compared to the virgin specimens. The reasons for the low impact toughness of the green specimens and inconsistency relative to literature however require further investigations.

3.6 Tensile Test

Representative strain-stress curves of the tensile measurements of the horizontal and vertical built specimens are shown in Fig. 16(a) for virgin and (b) for green specimens. The plots in Fig. 15(c) show the Z- built specimens of virgin (black curves) and the green specimens (blue curves) for comparison. To analyze the effects due to height along the BD, the tensile test of the top sections and bottom sections of the virgin material are presented in Fig. 16(d). The black coloured curves represent the bottom specimens whereas the red curves are for the specimens in the top section of the built rod. For comparison, the average values of the Ultimate Tensile Strength (UTS), Yield Strength (YS), and Elongation (El) of both virgin and green specimens are plotted and shown in Fig. 17. The labeled numbers shown are average values of X- Y- and Z- specimens. In both virgin and green, the X & Y (horizontally built) specimens have larger UTS and
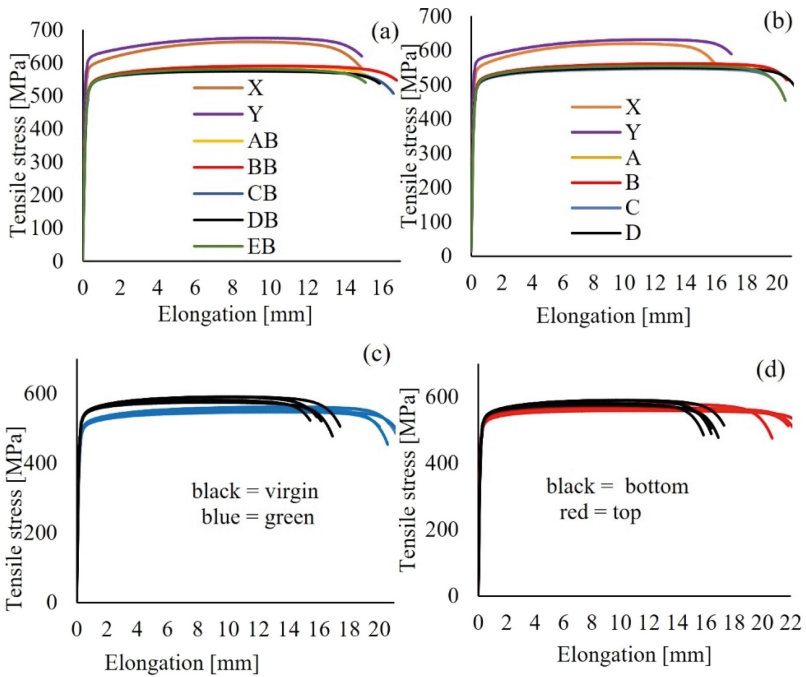

Fig. 16. Tensile test – (a) virgin (b) green, (c) Z-built specimens of virgin (black) and green (blue), and (d) top (black) and bottom (red) specimens of virgin specimens. Note that the plots for the bottom - virgin specimens are compared with that of green. A, B, C, D, and E specimens were built in the Z-orientation and printed at different locations as shown in Fig. 1. The subscript 'B' in the legend of (a) refers to 'bottom'.

YS 0.2% than the Z (vertically built) specimens. As expected, the Z- specimens have shown higher ductility in both virgin and green specimens.

Effects of Building Orientation

The average UTS of virgin specimens (Y) is larger than the X- and Z- specimens by 12 (2%) and 99 MPa (17%), respectively. Similarly, the average yield strength of Y- specimens is larger by about 12 (2%) and 77 MPa (15%) than that of X- and Z- specimens, respectively. The differences observed in both UTS and YS between Y- and Z- built as well as between X- and Z- built specimens are significant. As stated above, the specimens printed normal to the BD (horizontal) have shown larger strength than the specimens printed parallel to the BD (vertical).

The green specimens have also shown a similar tendency of variation in strength as that of the virgin specimens. The average values of UTS and YS of Y- green specimens are larger than the Z-specimens by 77 MPa (14%) and 86 MPa (19%), respectively. The differences between the measurements of UTS and YS of Y- and the X- specimens are not as pronounced as that of the Y- and Z- specimens as shown in Fig. 17. The elongation is however higher for the Z- specimen than the horizontally built specimens in both virgin and green specimens. The current observation is consistent with reports in the literature for 316L SS [38, 39]. Typical values reported [39–41] indicate that the UTS and YS of the horizontally built specimens are higher than the vertically built specimens of LPBF-manufactured 316L SS by about 16–22% and 19–28%, respectively.

The cause of mechanical anisotropy is often linked to the layer-by-layer manufacturing of parts by the LPB-F system pertaining to different orientations with respect to the applied stress. The observation shows that tensile strength becomes weaker when the thickness layers are oriented normal to the applied stress than when they are oriented parallel to the direction of applied stress. The extent of stresses accumulated is the cause for the weaker strength in the Z-built specimens than in the horizontally built specimens. This can be explained in terms of defect formation. In general, the orientations of the layers with respect to the applied tensile stress and the quantity of the layers are regarded as the key factors for the differences observed in the tensile strength between the two sets of specimens [40, 42]. According to Yadroitsev et al. [38], the vertically built specimens have numerous defects caused by a considerable amount of thermal stresses accumulated during the heating/cooling cycles than the horizontally built specimens. The stresses are mainly due to micro-segregation, oxidation, inclusions, unmelted powders or pores that occurred frequently at the interfaces between the layers normal to the build direction [40]. In addition, the Z-built specimens consist of more layers than those specimens built in the X- or Y- orientations. A larger number of layers and interfaces are under the stresses applied in the case of the specimens built in the vertical orientation than the specimens built in the horizontal orientation. Thus, the vertically built specimens resist fracture failure longer than the horizontally built specimens [32], and thus higher ductility. The anisotropy in ductility can then be associated with the anisotropic nature of the microstructure fabricated by LPBF.

Effects of Building Height on Tensile Strength

To assess differences (if any) in the tensile properties at different heights along the BD, the top and the bottom specimens of virgin material that were built in the Z-direction
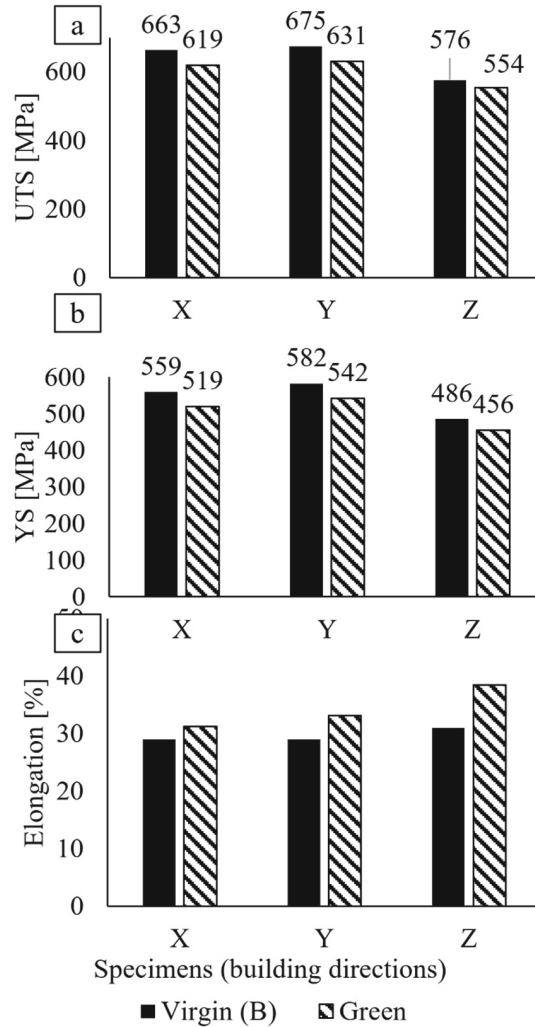
Fig. 17. Tensile strength measurement (a) UTS, (b) YS 0.2% and (c) elongation (E)

are compared. The UTS, YS, and ductility values are listed in Table 5. Relatively, the specimens in the bottom section have larger tensile and yield strength than the top section of the material. The maximum difference between these specimens in UTS is 2.9% and YS is 2.2%. The largest and smallest differences in YS observed between the bottom and the top specimens are about 11 MPa (E) and 1 MPa (A), respectively. Similarly, the largest and smallest differences in UTS are 16 MPa (D) and 10 MPa (A), respectively. As expected, the ductility of the top specimens is higher than the bottom specimens. The exception is specimen C, which showed almost the same elongation for both CT and CB despite differences of about 8 MPa in YS and 12 MPa in UTS. The slight variations shown in the mechanical strength between the top and bottom sections of specimens could be

due to differences in stresses. The layers at the bottom part endure more local heating-cooling cycles than the top part during the printing/solidification process. It means the lower part experiences more stress than the upper part of the cylindrical specimen. The stresses are usually associated with dislocations that are accountable for the variations in strength between the bottom and top sections of the vertically built specimens. Such stresses can be reduced or relieved by post-fabrication treatment, including solution heat treatment or hipping process.

Table 5. Tensile properties of the top (T) and the bottom (B) virgin specimens built in the Z-direction.

Specimens	YS 0,2% [MPa]	UTS [MPa]	El. [mm]
AT	481.9	579.5	22.0
AB	482.6	589.5	17.6
BT	487.2	579.5	25.5
BB	485.1	590.1	23.1
CT	480.4	561.8	25.1
CB	488.1	574.2	25.6
DT	485.4	558.7	25.8
DB	493.4	575.0	18.8
ET	480.7	567.6	25.4
EB	491.6	580.7	19.0
XX	558.9	663.0	19.5
YY	582.2	674.7	20.1
ZZ	485.6	575.7	22.8

Tensile Fracture

Figure 18 and 19 show SEM images of tensile fracture surfaces of some of the tested specimens. The images on the left column (a, c, and e) exhibit the whole fractures (both Figures) for Z, X and Y-built specimens (virgin) whereas, the right column (b, d, and f) shows images of the green specimens at different magnifications. The whole fractures in (a, d, and g) reveal a necked failure which generally indicates ductile fracture. Furthermore, close examination of the images reveals intergranular brittle fractures with variable shapes, sizes, and distributions of dimples. Some intergranular faceted fractures with variable dimensions are also seen.

Generally, the fracture surfaces consist of external defects, in particular crater-like pores of variable sizes (Fig. 18, 19), that can act as a site for crack initiation. Qualitative observation indicates the presence of a larger number of pores present in the green specimens than in the virgin as shown in Fig. 19. The size of the pores 'ranges from a few microns to 100 µm. Referring to Griffith's theory, Wang and his co-workers [43] based their argument by treating the pre-existing pores as surface cracks. With the application of tensile load that leads to deformation, the local stresses around the pre-existing pores exceed the fracture strength of the material and failed to withstand further stress. This results in the accumulation of high stresses around the pre-existing pores. The stresses are thus relaxed by the nucleation of multiple cracks around the pores. In this study, most of the cracks observed on the fracture surfaces are believed to be due to the propagation of the pre-existing microcracks (Fig. 9, 10). Moreover, the pre-existing pores can be the sites of crack initiations during tensile fracture.
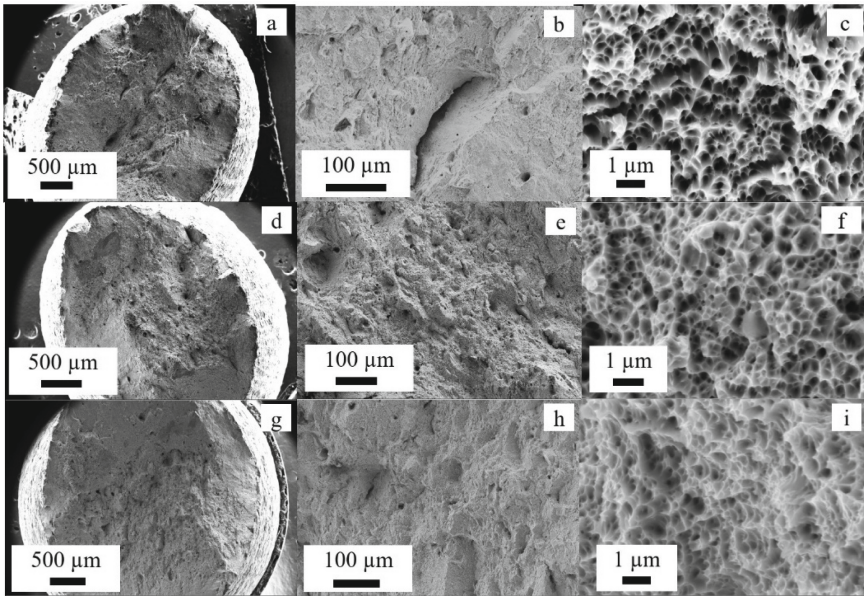

Fig. 18. Overall morphology of virgin specimen (a–c) Z-built (d–f) horizontal (X)-built and (g–i) horizontal-built (Y) specimens.

Virgin vs. Green

The measurement shows that the tensile strengths of the virgin specimens are larger than those of the green specimens in all categories. However, the ductility of the virgin specimens is low compared to the green specimens as shown in Fig. 16(c) and Fig. 17(c). The average UTS and YS of the virgin X- and Y-specimens are larger than those of the green by 7%, each. Similarly, the Z-built specimens of the virgin are larger in UTS by 4% and in YS by 7%, than the corresponding green specimens. The differences are however not so high. Several factors can be accountable for the differences in the mechanical
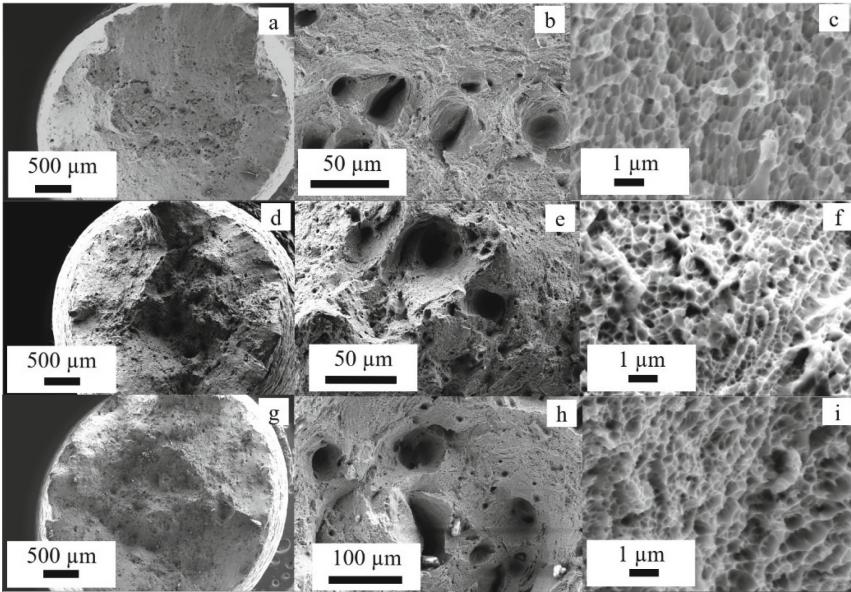
Fig. 19. Overall morphology of green specimens (a–c) Z-built (d–f) horizontal (X)-built and (g–i) horizontal-built (Y) specimens.

strength observed between the virgin and green parts. These can be related to the defects in the microstructure and the quality level of the powders. As shown above, qualitative observation of SEM images indicates that the green specimens show a larger number of defects than the virgin specimens. Microcracks are dominant in some of the green specimens. Although, the average surface porosity of the green specimens is smaller than that of the virgin specimens, the level is quite low ($<1\%$) for both specimens. The external defects essentially the microcracks and microvoids are believed to be the main causes for the differences observed in the tensile properties. Furthermore, the precipitation of a larger number of nano-oxides in the virgin material has a positive effect on the tensile strength compared to the green specimens. Besides dislocations, as indicated by Zhong et al. [44], the pinning effect due to nano-oxides can hinder the crack propagation or deformation to strengthen the tensile property. Detailed quantitative analysis (e.g., sphericity) are required to justify the quality level of the green powders.

For comparison, it is worthy to refer to a list of tensile properties of 316L SS fabricated by various AM techniques compiled in a review paper by Saboori et al. [45]. As shown in the list, besides differences in AM methods employed, the specimens studied were fabricated under various conditions (e.g., process parameters, and building orientations). Despite that as the list [45] shows, the UTS of the austenite 316L SS lies in the range of 536 and 690 MPa. The values for the YS 0.2% lie between 352 and 610 MPa. As shown in Fig. 17, the range of UTS of the virgin and the green specimens in the current work are 576–675 MPa and 554–631 MPa, respectively. Similarly, the range of YS 0.2% measured for virgin specimens is 486–582 MPa and 456 -519 MPa for green specimens. These show that the values from the current work for both types of specimens are consistent

with the values reported in the literature for similar alloy components built using the virgin powder.

4   Conclusions and Vision

This work investigated and compared the microstructure and mechanical strength of LPBF-fabricated specimens of green and virgin powders of 316L SS. The following conclusions are made based on the analysis.

- The powder particles made from green material of 316L SS have nearly spherical shapes and sizes like the virgin powder particles. The particle size distribution (PSD) of virgin powder shifts to the higher particle size, indicating a slightly larger average particle size compared to that of green material.
- The green specimens showed slightly lower mechanical strength compared to the virgin specimens. The highest average hardness of virgin (230 HV) and green (223 HV) are observed on the surfaces normal to the BD. Lower defect levels and a larger number of oxides nanoprecipitates contribute to the higher values of hardness in virgin specimens.
- The grain structure of the specimens printed from powder manufactured from green material is identical to that of the specimens printed from fresh powder. There is however slightly larger number of external defects such as microcracks in the powder fabricated from the green than in the virgin.
- The mechanical properties of LPBF-built 316L SS showed a strong dependency on the specimens' building directions. The UTS and YS of the horizontally built specimens (Y-virgin) are larger than the Z- specimens by 17% and 15%, respectively. Similarly, the horizontally built green specimen is larger than the vertically built specimen by 14% (UTS) and 19% (YS). The anisotropy in the mechanical strength is supposed to be due to anisotropy in the microstructure.
- The average UTS and YS of the horizontally built virgin specimens are larger than the green specimens by 7%. Similarly, the Z-built specimens of the virgin are larger in UTS by 4% and in YS by 7%, than the green specimens. The pre-existing external defects, including microcracks and microvoids, are believed to be accountable for the slight reduction of mechanical strength of the specimens from a green material. The upcoming research focuses on identifying the causes and minimizing such defects.
- The hardness (223 HV (g), 230 HV (v)), UTS (631 MPa (s), 675 MPa (v)) and YS (54 MPa (g), 582 MPa (v)) and ductility (18% (g), (16% (v)) of the horizontally built (Y) specimens are not significantly differing although the variations are larger for the other specimens built in the X and Z orientations. This demonstrates that the specimens fabricated from the powders of 316L SS greens meet the standard production requirements, but further work is required to attain optimum conditions (e.g., mechanical strength, toughness).

References

1. du Plessis, A., Yadroitsava, I., Yadroitsev, I.: Effects of defects on mechanical properties in metal additive manufacturing: a review focusing on X-ray tomography insights. Mater. Design **187** (2020)
2. Malekipour, E., El-Mounayri, H.: Common defects and contributing parameters in powder bed fusion AM process and their classification for online monitoring and control: a review. Int. J. Adv. Manuf. Technol. **95**(1–4), 527–550 (2017)
3. Tucho, W.M., Lysne, V.H., Austbø, H., Sjolyst-Kverneland, A., Hansen, V.: Investigation of effects of process parameters on microstructure and hardness of SLM manufactured SS316L. J. Alloy. Compd. **740**, 910–925 (2018)
4. Ostovan, F., Shafiei, E., Toozandehjani, M., Mohamed, I.F., Soltani, M.: On the role of molybdenum on the microstructural, mechanical and corrosion properties of the GTAW AISI 316 stainless steel welds. J. Market. Res. **13**, 2115–2125 (2021)
5. Mat Noor, F., Jamaludin, K.R., Ahmad, S.: Physical and mechanical characteristics of porous SS316L for biomedical implant. Solid State Phenomena **268**, 374–378 (2017)
6. Hajnys, J., Pagac, M., Mesicek, J., Petru, J., Spalek, F.: Research of 316L metallic powder for use in SLM 3D printing. Adv. Mater. Sci. **20**(1), 5–15 (2020)
7. Liu, B., Wildman, R.D., Tuck, C.J., Ashcroft, I.A., Hague, R.J.M.: Investigation the effect of particle size distribution on processing parameters optimisation in selective laser melting process (2011)
8. Sutton, A.T., Kriewall, C.S., Leu, M.C., Newkirk, J.W.: Powder characterisation techniques and effects of powder characteristics on part properties in powder-bed fusion processes. Virtual Phys. Prototyping **12**(1), 3–29 (2017)
9. Simmons, J.C., et al.: Influence of processing and microstructure on the local and bulk thermal conductivity of selective laser melted 316L stainless steel. Addit. Manuf. **32**, 100996 (2020)
10. Strondl, A., Lyckfeldt, O., Brodin, H., Ackelid, U.: Characterization and control of powder properties for additive manufacturing. JOM **67**(3), 549–554 (2015)
11. Tang, H.P., Qian, M., Liu, N., Zhang, X.Z., Yang, G.Y., Wang, J.: Effect of powder reuse times on additive manufacturing of Ti-6Al-4V by selective electron beam melting. JOM **67**(3), 555–563 (2015)
12. Cordova, L., Campos, M., Tinga, T.: Revealing the effects of powder reuse for selective laser melting by powder characterization. Jom **71**(3), 1062–1072 (2019)
13. Mohd Yusuf, S., Choo, E., Gao, N.: Comparison between virgin and recycled 316L SS and AlSi10Mg powders used for laser powder bed fusion additive manufacturing. Metals **10**(12), 1625 (2020)
14. Gorji, N.E., O'Connor, R., Mussatto, A., Snelgrove, M., González, P.G.M., Brabazon, D.: Recyclability of stainless steel (316 L) powder within the additive manufacturing process. Materialia **8** (2019)
15. Li, S., Chen, B., Tan, C., Song, X.: Study on recyclability of 316L stainless steel powder by using laser directed energy deposition. J. Mater. Eng. Perform. (2021)
16. Sustainability in steel recycling (2020). https://www.steel.org/. Accessed 10 Mar 2022
17. Zhang, J., et al.: Comparison of virgin and reused 15-5 PH stainless steel powders for laser powder bed fusion process. Progr. Addit. Manuf. **3**(1), 11–14 (2018)
18. Sendino, S., Martinez, S., Lamikiz, A.: Characterization of IN718 recycling powder and its effect on LPBF manufactured parts. Procedia CIRP **94**, 227–232 (2020)
19. Laurentiu Nastac, J.J.V., Tims, M., Dax, F.R.: Advances in the solidification on IN718 and RS5 alloys. In: Loria, E.A. (ed.) Superalloys 718, 625, 706, and Various Derivatives, The Mlnerals. Metals and Materials Society, Johnstown, PA (2001)

20. Nastac, L., Tims, M.L., Dax, F.R., Concurrent, I.: Advances in the solidification of IN718 and RS5 alloys. Superalloys 103–112 (2001)
21. Niendorf, T., Leuders, S., Riemer, A., Richard, H.A., Tröster, T., Schwarze, D.: Highly anisotropic steel processed by selective laser melting. Metall. and Mater. Trans. B. **44**(4), 794–796 (2013)
22. Tucho, W.M., Cuvillier, P., Sjolyst-Kverneland, A., Hansen, V.: Microstructure and hardness studies of Inconel 718 manufactured by selective laser melting before and after solution heat treatment. Mater. Sci. Eng., A **689**, 220–232 (2017)
23. Tucho, W.M., Hansen, V.: Studies of post-fabrication heat treatment of L-PBF-inconel 718: effects of hold time on microstructure, annealing twins, and hardness. Metals **11**(2) (2021)
24. Zhang, B., Li, Y., Bai, Q.: Defect formation mechanisms in selective laser melting: a review. Chin. J. Mech. Eng. **30**(3), 515–527 (2017)
25. Zhang, S.: Cracking behavior and formation mechanism of TC4 alloy formed by selective laser melting. J. Mech. Eng. **49**, 21 (2013)
26. Gu, D., et al.: Densification behavior, microstructure evolution, and wear performance of selective laser melting processed commercially pure titanium. Acta Mater. **60**(9), 3849–3860 (2012)
27. Read, N., Wang, W., Essa, K., Attallah, M.M.: Selective laser melting of AlSi10Mg alloy: process optimisation and mechanical properties development. Mater. Design (1980–2015) **65**, 417–424 (2015)
28. Shen, Y.F., Gu, D.D., Wu, P.: Development of porous 316L stainless steel with controllable microcellular features using selective laser melting. Mater. Sci. Technol. **24**(12), 1501–1505 (2008)
29. Sames, W.J., List, F.A., Pannala, S., Dehoff, R.R., Babu, S.S.: The metallurgy and processing science of metal additive manufacturing. Int. Mater. Rev. **61**(5), 315–360 (2016)
30. Yusuf, S.M., Chen, Y., Boardman, R., Yang, S., Gao, N.: Investigation on porosity and microhardness of 316L stainless steel fabricated by selective laser melting. Metals **7**(2), 64 (2017)
31. Leung, C.L.A., Marussi, S., Towrie, M., Atwood, R.C., Withers, P.J., Lee, P.D.: The effect of powder oxidation on defect formation in laser additive manufacturing. Acta Mater. **166**, 294–305 (2019)
32. Chen, J., Hou, W., Wang, X., Chu, S., Yang, Z.: Microstructure, porosity and mechanical properties of selective laser melted AlSi10Mg. Chin. J. Aeronaut. **33**(7), 2043–2054 (2020)
33. Sun, Z., Tan, X., Tor, S.B., Yeong, W.Y.: Selective laser melting of stainless steel 316L with low porosity and high build rates. Mater. Des. **104**, 197–204 (2016)
34. Saeidi, K., Kvetková, L., Lofaj, F., Shen, Z.: Austenitic stainless steel strengthened by the in situ formation of oxide nanoinclusions. RSC Adv. **5**, 20747–20750 (2015)
35. Pavlina, E.J., Van Tyne, C.J.: Correlation of yield strength and tensile strength with hardness for steels. J. Mater. Eng. Perform. **17**(6), 888–893 (2008)
36. Neikter, M., Raja, D.C., Balachandramurthi, A.R., Harlin, P.: Tailored ductility and strength for enhanced impact toughness of laser powder fusion built Alloy 718. J. Alloys Compounds **884** (2021)
37. Fu, J., Zhang, Y.: Mechanism of crack initiation and propagation of 316LN stainless steel during the high temperature tensile deformation. Mater. Res. Express **7**(8), 085801 (2020)
38. Yadroitsev, I., Thivillon, L., Bertrand, P., Smurov, I.: Strategy of manufacturing components with designed internal structure by selective laser melting of metallic powder. Appl. Surf. Sci. **254**(4), 980–983 (2007)
39. Casati, R., Lemke, J., Vedani, M.: Microstructure and fracture behavior of 316L austenitic stainless steel produced by selective laser melting. J. Mater. Sci. Technol. **32**(8), 738–744 (2016)

40. Mertens, A., et al.: Mechanical properties of alloy Ti-6AI-4V and of stainless steel 316L processed by selective laser melting: influence of out-of-equilibrium microstructures. Powder Metall. **57**, 184–189 (2014)
41. Pitrmuc, Z., et al.: Mechanical and microstructural anisotropy of laser powder bed fusion 316L stainless steel. Materials **15**(2), 551 (2022)
42. Röttger, A., et al.: Microstructure and mechanical properties of 316L austenitic stainless steel processed by different SLM devices. Int. J. Adv. Manuf. Technol. **108**(3), 769–783 (2020)
43. Wang, Z., et al.: Premature failure of an additively manufactured material. NPG Asia Mater. **12**(1), 30 (2020)
44. Zhong, Y., Liu, L., Wikman, S., Cui, D., Shen, Z.: Intragranular cellular segregation network structure strengthening 316L stainless steel prepared by selective laser melting. J. Nucl. Mater. **470**, 170–178 (2016)
45. Saboori, A., Aversa, A., Marchese, G., Biamino, S., Lombardi, M., Fino, P.: Microstructure and mechanical properties of AISI 316L produced by directed energy deposition-based additive manufacturing: a review. Appl. Sci. **10**(9), 3310 (2020)